

Cross-Shelf Eddy Heat Transport in a
Wind-Free Coastal Ocean Undergoing Winter
Time Cooling

James M. Pringle

Woods Hole Oceanographic Institution

Woods Hole Ma. 02543

September 20, 2000

Current Address:
James M. Pringle,
SIO-UCSD, Mail stop 0218
La Jolla, Ca. 92093-0218
jmpringle@ucsd.edu

Abstract

A steady-state cross-shelf density gradient of a wind-free coastal ocean undergoing winter time cooling is found for cooling and geometries which do not vary in the alongshelf direction. The steady-state cross-shelf density gradient exists even when the average density of the water continues to increase. The steady-state density gradient can be attained in less than a winter for parameters appropriate to the mid-Atlantic Bight. The cross-shelf eddy driven buoyancy fluxes which cause this steady-state gradient are found to depend critically on bottom friction and bottom slope, and the coastal polyna solutions of *Chapman and Gawarkiewicz* [1997] are significantly modified by this dependence in the limit of polynas with a large alongshore extent. Bottom friction retards the cross-shelf propagation of eddies, so that the buoyancy transport is no longer carried by self-advecting eddy-pairs, but mixed across the shelf by interacting eddies. The eddy interaction changes the length scale of the eddies until it is the lesser of the Rhines arrest scale or an analogous frictional arrest scale. The estimates of the steady-state cross-shelf density gradient are found to compare well with numerical model results.

1 Introduction

In the winter, an ice free coastal ocean is cooled by the atmosphere over length scales large compared to the shelf width or an internal radius of deformation. This cooling makes shallow waters colder than deeper waters, causing a density gradient which tends to increase as the cooling persists. At the same time, the cross-shelf heat flux driven by these density gradients tend to reduce the density gradients. Numerical and scaling solutions are given below in which the tendency of atmospheric cooling to increase the mean cross-shelf density gradient is balanced by the tendency of the cross-shelf eddy heat fluxes to reduce the gradient, and the cross-shelf density gradient reaches a steady-state.

Several recent works have examined problems of a similar nature: *Visbeck et al.* [1996], hereafter VMJ, study the response of a deep, open ocean to localized cooling, which models the response of a locally preconditioned ocean to large scale cooling events [*Legg et al.*, 1998]. *Chapman and Gawarkiewicz* [1997], hereafter CG, study the response of a coastal ocean to isolated cooling near the coast, in order to model a polar ocean with an isolated ice free region next to the shore. Both of these works find that the water beneath the cooling region reaches a steady-state density and successfully predict that density.

Spall and Chapman [1998] show that the steady-state density occurs when pairs of eddies advect themselves away from the cooling region, carrying dense water away from the cooling region. This horizontal buoyancy flux away from the cooling region increases as the density of the cooled region increases, and a steady-state density is reached when the horizontal flux out of the cooling region balances the vertical flux into the cooling region such that the density no longer increases.

It is found below, however, that adding realistic levels of bottom friction fundamentally changes the results of CG, at least in the limit of a polyna of infinite alongshore extent. The bottom friction prevents the propagation of eddies away from the cooling region, forcing them to interact. Similarly, eddies are forced to interact in an ice free coastal ocean because the horizontal density gradients which form the eddies can exist for many eddy length scales across the shelf. The eddies thus form everywhere and in close proximity to each other and interact. The interacting eddies merge, cascade to larger scales, and form a turbulent flow which mixes heat across the shelf. The cross-shelf buoyancy flux driven by this eddy mixing increases as the cross-shelf density gradient increases, and a steady-state cross-shelf density gradient is reached when the horizontal flux away from the coast balances

the vertical flux into the surface such that the horizontal density gradient no longer increases.

It will be argued below that this steady-state horizontal density gradient does not imply a steady-state density. To the contrary, even in a semi-infinite model of the coastal ocean, the density will tend to increase without bound. If the coastal ocean is not semi-infinite, the mean density of the coastal waters will only depend on the surface flux and the cross-shelfbreak flux of buoyancy. The work below confines itself to the dynamics of the coastal ocean, and assumes the cross-shelfbreak flux of buoyancy is given. Even if the given cross-shelfbreak flux does not balance the surface cooling and the density increases without bound, the cross-shelf density gradient reaches a steady-state. For this reason, it will be the steady-state cross-shelf density gradient which will be sought. Since it is the density gradient, not the density, which force the currents and control mixing on the shelf, a steady-state density gradient implies steady mean currents, steady cross-shelf transport and dispersion, and steadiness in all important motions and quantities on the shelf save the actual density.

In order to motivate the derivation of an estimate for the steady state cross-shelf density gradient, two numerical model runs are presented, one

with parameters appropriate for the mid-Atlantic Bight in winter, and another based on the model runs of CG but with a polyna of infinite alongshelf extent and with bottom friction. Following this is a derivation of an estimate for the steady-state cross-shelf density gradient. The derivation is then compared to an ensemble of model runs with differing forcings and geometries, and the successes and limitations of the scaling presented.

In none of the scalings derived below, and in none of the model runs shown, is the geometry or forcing allowed to vary in the alongshelf direction—only the flow fields are allowed to vary alongshelf. The problem of alongshelf heat fluxes, parallel to isobaths instead of across them, is not considered below.

2 A numerical model run motivated by the mid-Atlantic Bight

The physics important to the winter time mid-Atlantic Bight, excluding wind, can be modeled crudely by a periodic channel with a linear bottom slope of 10^{-3} between a depth of 10 m and a 170 m (figure 1), and a uniform surface buoyancy loss B of $7 \times 10^{-8} \text{ m}^2 \text{ s}^{-3}$, which is equivalent to a heat

loss of 300 W m^{-2} from 3°C water or 170 W m^{-2} from 10°C water. Both the geometry and cooling are appropriate for the northeast coast of North America [*Brown and Beardsley, 1978; Mountain et al., 1996*]. No bouyancy leaves the domain through the horizontal boundaries (runs are made below which include an open offshore boundary). The numerical model, SPEM 5.1, is a primitive equation, modified sigma coordinate, hydrostatic model. The effects of convection will be represented by an enhanced vertical diffusivity wherever the stratification is unstable, because the physics of convection cannot be represented accurately by the hydrostatic model. The vertical walls have free slip boundary conditions. Other details of the model, convective adjustment, and forcing are given in the appendix.

When cooling is imposed on the initially homogeneous water of the model, convection mixes the water from top to bottom in less then an inertial period ($2\pi f^{-1}$), and keeps the entire water column slightly unstably stratified. This strong vertical mixing inhibits the cross-shelf flux of heat while preventing the earth's rotation from strongly affecting the flow [*Pringle, 1998*]. During this regime, the cross-shelf heat transport is small, the heat balance is essentially

one dimensional, and the vertical mean density $\bar{\rho}$ evolves as

$$\bar{\rho} = \frac{\rho_0 B t}{g h}, \quad (1)$$

where h is the water depth, g the gravitational acceleration, and ρ_0 the mean density. Since there is a bottom slope, there is a cross-shelf density gradient which drives a weak ($< 1 \text{ cm s}^{-1}$) cross-shelf flow [*Pringle*, 1998]. The top panels of figure 2 shows the density field in the model run during this convection dominated regime, at $t = 40$ days.

Pringle [1998] shows how the cross-shelf flow v driven by the cross-shelf density gradient forces the water column to become stably stratified, in this particular run after 40 days of cooling. The stable stratification reduces mixing at the base of the water column and allows rotation to affect the dynamics, allowing alongshore flow in thermal wind balance and baroclinic instabilities to form. The onset of the instabilities is shown in the middle panel of figure 2. Even before this time, a several day interruption of the cooling, and thus the vertical mixing, can allow along-shore flows and baroclinic instabilities to form.

Once instabilities in the flow form, they quickly start to transport heat

across the shelf, reducing the cross-shelf density gradient by 40% in 15 days. Soon after, the cross-shelf density gradient achieves a statistical steady-state, shown in figures 2c and 3, in which surface cooling is balanced by a cross-shelf heat flux. It is for this steady-state density gradient that the scaling below solves. Because there is a wall for the “offshore” boundary, and the surface is everywhere cooled, the mean density of the domain will always increase. However, the density will increase everywhere at the same rate, so the mean cross-shelf density gradient does not change. Not only does the cross-shelf density gradient reach a statistical steady-state, but the mean alongshore velocities, the length scales of the eddies, and the variance of the velocities all reach statistically steady-states. The flow at this point appears turbulent in the sense that the fluctuations in the flow at a point are unpredictable, and Lagrangian particles disperse as would be expected in a turbulent flow [Davis, 1987].

3 A numerical model motivated by a coastal polyna

In an ice covered coastal ocean, the wind can create gaps in the ice near the shoreline by blowing the ice offshore. These open patches of water can experience large surface buoyancy fluxes, both from cooling and from brine rejection. CG examine eddy buoyancy fluxes out of the ice-free region and give scales for the maximum density attained by the water beneath the polyna and the time needed to achieve this density in the limit of no bottom friction.

To examine how these dynamics are changed by bottom friction in the limit of a polyna with alongshelf extent much greater than its cross-shore extent, two model runs are made with the cooling limited to the 10 kilometers nearest to the shore, one with bottom friction, one without. The bottom is flat, with a depth of 100 meters, and the surface buoyancy flux B is about double the base case of CG, or $10^{-6}\text{m}^2\text{s}^{-3}$. As in CG, the offshore wall is placed far enough offshore that it does not affect the results shown in this section, so the domain is effectively semi-infinite (this is tested by repeating runs with the wall farther offshore). In the notation of CG and *Chapman* [1998], this is $a \gg b$, $b = 10\text{km}$, $W = L_d$, $H = 100\text{m}$, and $B_0 = 10^{-6}\text{m}^2\text{s}^{-3}$.

In the runs with bottom friction, the bottom stress is proportional to $\rho_0 r$ times the bottom velocity, and $r = 4.5 \times 10^{-4} \text{ m s}^{-1}$.

Spall and Chapman [1998] and *Chapman* [1998] predict that the density averaged over the cooling region will stop increasing at a time

$$t_{steady} \approx \left(\frac{2}{c_e}\right)^{\frac{2}{3}} \left(\frac{y_{cool}^2}{B}\right)^{\frac{1}{3}}, \quad (2)$$

after which the surface buoyancy flux is balanced by horizontal eddy buoyancy fluxes out of the cooling region. The constant c_e is found on theoretical grounds to be about 0.04 by *Spall and Chapman* [1998]. y_{cool} is the offshore extent of the cooling.

In figure 4, the evolution of the mean density of the cooling region is plotted for the two numerical model runs. In the model run without bottom friction, the density averaged over the cooling region is seen to reach a nearly steady-state of about 0.4 kg m^{-3} at day 8, which agrees well with the prediction of *Spall and Chapman* [1998]. The very small upward trend in the density after day 8 occurs because the lateral diffusion of temperature slightly cools the water entering the cooling region to replace the water removed by eddies.

In the numerical model run with bottom friction, however, the density in the cooling region does not reach a steady-state at the time predicted by (2), as only part of the surface cooling is balanced by a cross-shelf eddy driven heat flux. What is different in the frictional case? *Spall and Chapman* [1998] explain the steady-state density, and *a priori* derive c_e , by assuming buoyancy is carried away from the cooling region by counter-rotating vertically- and horizontally-offset pairs of eddies. These eddy pairs form a self-propagating system, a heton, which can move itself, and the dense water it carries, away from the cooling region at a speed of c_e times the swirl velocity. [*Hogg and Stommel*, 1985; *Legg et al.*, 1996]. This is illustrated in the top panels of figure 5. In the model of heton propagation by *Hogg and Stommel* [1985] either of these eddies alone would not propagate horizontally, but the pair together does. Bottom friction disrupts the heton by consuming the bottom eddy, leaving the surface intensified eddy unable to propagate across the shelf. The surface intensified eddy is then trapped, unable to escape the cooling region and thus unable to balance the surface buoyancy flux. This is illustrated in the lower panel of figure 5. (A similar mechanism for disrupting heton propagation over a frictionless but sloping bottom is given in *LaCasce* [1996].)

Bottom friction will retard the cross-shelf propagation of hetons within a friction time scale (h/r) of their generation, where r is the coefficient of a linear bottom drag law. This friction time scale is about 2.5 days in the bottom friction case, short compared to the time scale for the achievement of a steady-state density in the cooling region, (2). It is thus unlikely that heton dynamics are ever important in the run with bottom friction. Deprived of their ability to propagate across the shelf, these eddies remain near to their source and begin to interact, forming a turbulent flow which mixes density across the shelf. In fully spun up runs with bottom friction, the eddies neither propagate far, nor propagate in a consistent direction across the shelf, before they are sheared apart by other eddies (Figure 6). When a patch of passive tracer was placed in the flow, the dispersion of the patch increased in a manner consistent with turbulent mixing processes [*Pringle*, 1998].

The density at the coast evolves in a fundamentally different manner when dense water is mixed across the shelf instead of being transported across the shelf by self-propelled eddy pairs. The flux of buoyancy across the shelf by the eddy pairs, as described in *Spall and Chapman* [1998], is a function of the density anomaly of the cooling region— thus in the frictionless model the density anomaly increases until it drives a flux sufficient to prevent the

density anomaly from increasing further. The cross-shelf buoyancy flux in the frictional sloping bottom model is shown below to be a function of the cross-shelf density gradient – thus the cross-shelf density gradient increases until it drives a buoyancy flux sufficient to prevent the cross-shelf density gradient from increasing further. Since it is density gradients which drive cross- and along-shelf currents and mixing, these too are in a steady state. However, a steady-state density gradient does not imply a steady-state density. This can be seen most easily in the simple case of a cross-shelf buoyancy flux which depends linearly on the cross-shelf density gradient (*i.e.* a constant eddy diffusivity). In a semi-infinite ocean, the density at the coast will then increase as the square root of time. This is because, for a constant eddy diffusivity, the offshore extent of the buoyancy anomaly will scale as the square root of time. The total buoyancy in the ocean anomaly will scale as the buoyancy at the coast times the offshore extent of the buoyancy anomaly, and must also increase linearly with time as the surface buoyancy flux is constant– thus the anomaly at the coast will increase as the square root of time (*c.f.* *Kevorkian* [1990] p. 22). It is straightforward to extend this result and show that the buoyancy anomaly at an arbitrary point will also increase as the square root of time at long time if the cross-shelf buoyancy

flux scales as the cross-shelf density gradient raised to any non-zero power. In a semi-infinite ocean, the cross-shelf buoyancy flux at a point differs from the net surface flux inshore of that point by an amount proportional to the time rate of change of the average buoyancy inshore of that point. Since the buoyancy increases as the square root of time, the cross-shelf buoyancy flux will asymptote to a constant as one over the square root of time at long time.

4 The scaling for the steady-state Cross-shelf density gradient: Introduction

In the preceding section, numerical model results were shown that described the evolution of a coastal ocean from a homogeneous body of water to a stratified ocean with a statistically steady cross-shelf density gradient. This steady density gradient is sufficient to drive a cross-shelf buoyancy flux which balances the surface cooling. The eddies which produced the mixing that caused the cross-shelf buoyancy flux were formed and destroyed with little cross-shelf translation: thus, presumably, the dynamics of the eddies depends on local conditions.

The scalings below solve for the resulting cross-shelf density gradient in

three steps: First, given the distribution of the surface buoyancy flux, the cross-shelf buoyancy flux for a steady-state buoyancy (and hence density) *gradient* is diagnosed. Second, a scale is found relating the cross-shelf density gradient to the cross-shelf buoyancy flux it causes. Third, these two steps are combined algebraically to find the cross-shelf density gradient.

4.1 Buoyancy/Heat Balance

The first step in solving for the steady-state is to find the cross-shelf buoyancy flux which leaves the cross-shelf density gradient in steady state. To make the following derivations simpler, the Boussinesq approximation is made and a linear equation of state will be assumed, allowing either cooling or brine rejection to be included in a single equation for the conservation of density:

$$\frac{\partial \bar{\rho}}{\partial t} + \frac{1}{h} \frac{\partial F}{\partial y} = \frac{\rho_0 B}{gh}. \quad (3)$$

The overbar is a depth and alongshelf averaging operator, F is the depth integrated cross-shelf flux

$$F \equiv h \bar{v} \bar{\rho}, \quad (4)$$

and B is the surface buoyancy flux. (Details of the conversion of a heat flux to B are given in the appendix.)

For the buoyancy balance to be in steady-state, the eddy currents which mix the buoyancy across the shelf must be in a statistically steady-state. For the currents to be in a statistically steady-state, the cross-shelf density gradient which drive them must also be in a statistically steady-state. For the cross-shelf density gradient to be in a steady-state, the time rate of change of density must be the same everywhere on the shelf. Thus the derivation below solves for the cross-shelf density flux which causes the time rate of change of density, $\partial\rho/\partial t$, to be constant across the shelf. The flux at the seaward edge of the shelf, $F_0 = F(y_0)$, is assumed to be known, and the flux at the coast must be zero. These three conditions taken together allow (3) to be solved:

$$\frac{\partial\bar{\rho}}{\partial t} = \left(\int_0^{y_0} gB(y)\rho_0^{-1}dy - F_0 \right) \left(\int_0^{y_0} h(y)dy \right)^{-1}, \quad (5a)$$

$$F = \int_0^y gB(y)\rho_0^{-1}dy - \frac{\partial\bar{\rho}}{\partial t} \int_0^y h(y)dy. \quad (5b)$$

Assuming that the cross-shelf flux at the seaward side of the domain is known is clearly artificial, but making that assumption allows one to focus on the processes occurring on the shelf. It is important to note that unless the cross-

shelf heat flux at the oceanward boundary exactly matches the cross-shelf integral of the surface cooling, the mean density of the water over the shelf changes with time. This in no way precludes the existence of a statistically steady cross-shelf density *gradient*.

4.2 Relating $\partial\bar{\rho}/\partial y$ to F

The second step towards finding the steady cross-shelf density gradient is to find the cross-shelf flux F driven by a known cross-shelf density gradient.

The cross-shelf depth integrated density flux F can be written

$$F = h\bar{v}\bar{\rho}, \quad (6)$$

and the flux can be scaled as

$$F = h\gamma V^* \rho^*, \quad (7a)$$

$$\rho^* = \bar{\rho}_y L^*, \quad (7b)$$

where V^* is a cross-shelf velocity scale, ρ^* is a density anomaly scale, $\bar{\rho}_y$ is the alongshelf averaged cross-shelf gradient in the depth-mean density, L^* is the cross-shelf length scale of the eddies which transport heat across the shelf,

and γ is the correlation between the depth averaged cross-shelf velocity and the depth averaged density field. Note that γ will not be used as a fitting parameter in this work. Equation (7) is a classical turbulent mixing scale; the restrictions on a flow field needed for it to be valid is given in *Davis* [1987]. It also assumes that the flux is the product of the depth averaged velocity times the depth averaged density anomaly and that the transport carried by the mean overturning circulation is small, an assumption whose validity is examined in section 5.

4.2.1 The Velocity Scale V^*

The velocity scale is

$$V^* = \frac{gh}{\rho_0 f} \overline{\rho_y}, \quad (8)$$

which assumes that the cross-shelf velocity perturbation scales as the mean alongshelf thermal wind velocity, and that the bottom Ekman layer occupies a negligible fraction of the water column. This assumption is traditionally justified by invoking an equipartition of kinetic and potential energy in the instability, which is the same as assuming that the length scale of the instabilities is the radius of deformation [*Visbeck et al.*, 1996]. Since, in general,

the length scales found below are not the radius of deformation, this argument is not very convincing in this case. When V^* is compared with the velocities in the numerical model runs presented in section 5, it is found to vary with the Burger number as would be expected from *Pedlosky* [1987], p. 374 eq. 6.10.27. Unfortunately, I have not been able to find a scale for the Burger number in the present case. This frustrates the effort to find a truly *a priori* scale for the cross-shelf buoyancy flux forced by geostrophic turbulence. There is some hope in deriving a rigorous upper bound on V^* by the method of *Shepherd* [1988] but with a more realistic dissipation scheme (*c.f.* *Held and Larichev* [1995], *Stone* [1972]). For now, however, the scale must be regarded as an *ad hoc* assumption with a good pedigree [*Chapman*, 1998; *Chapman and Gawarkiewicz*, 1997; *Stone*, 1972, VMJ].

4.2.2 The Correlation Between v and ρ : γ

The theoretical basis for choosing a correlation between the cross-shelf velocity and the density perturbation is currently limited to linear instability theory, but it is unclear what relevance linear instability theory has to finite amplitude eddies. It is not unreasonable, however, to expect the linear instability analysis to capture approximately the dynamics of the eddies, and

several authors have gone so far as to base eddy turbulence closure schemes on the linear instability solutions [Killworth, 1998; Stone, 1972]. *Blumsack and Gierasch* [1972] have performed a linear stability analysis for an Eady instability over a sloping bottom, and found a correlation coefficient γ which varies from ≈ 0.4 for a flat bottom to a maximum of ≈ 0.7 for a bottom slope half that of the isopycnal slope. (The value of γ is very different from the value of c_e found by *Spall and Chapman* [1998] and used in VMJ and CG because the underlying processes they represent are very different. c_e is the ratio of the swirl speed of an eddy to the propagation speed of a heton pair, while γ is the correlation between the depth averaged density anomaly and depth averaged velocity in a turbulent flow.)

4.2.3 The Cross-Shelf Length Scale L^*

Simply choosing the radius of deformation or the wavelength of the most unstable mode for the length scale L^* ignores much work that describes a cascade to larger horizontal and vertical scales in dense eddy fields. *Rhines* [1977], *Held and Larichev* [1995], and *LaCasce* [1996] show that in inviscid flows where the internal radius of deformation L_d is less than the Rhines arrest scale L_{Rh} , a turbulent flow will experience a cascade to larger horizontal

and vertical scales until the cross-shelf length scale is the Rhines arrest scale:

$$L_{Rh} = \sqrt{\frac{2V^*}{\beta}}, \quad (9)$$

where β is the planetary or topographic vorticity gradient

$$\beta = \frac{f}{h} \frac{\partial h}{\partial y}. \quad (10)$$

This scale is most easily understood as the length at which advective terms in the quasigeostrophic potential vorticity equations becomes smaller than the topographic β term. Once the length scale of the flow have increased to L_{Rh} , linear terms balance the non-linear terms, thus preventing a further cascade to large scales [*Pedlosky*, 1987, p. 174]. Thus one candidate for the cross-shelf length scale of the eddies is L_{Rh} .

However, the time scale of the cascade of energy to larger scales, and the time scale for the conversion of potential to kinetic energy, is

$$\mathcal{T}_{advect} = \frac{L^*}{V^*} \quad (11)$$

[*Pedlosky*, 1987, p. 174]. The time scale for the dissipation by bottom friction

of eddies where $L^* \gg L_d$ is

$$\mathcal{T}_{fric} = \frac{h}{r}, \quad (12)$$

where r is the friction coefficient for a linear drag law of the form $\vec{\tau} = \rho_0 r \vec{u}$ [St-Maurice and Veronis, 1975]. If $\mathcal{T}_{advec} > \mathcal{T}_{fric}$, the energy at the largest scales would be dissipated by bottom friction faster than energy could cascade to that scale. If the choice of $L^* = L_{Rh}$ caused $\mathcal{T}_{advec} > \mathcal{T}_{fric}$ it is improbable that L_{Rh} could be the length scale, and instead it seems probable that the energy-containing scale would be the one for which the conversion of potential energy to kinetic would be balanced by the dissipation of kinetic energy by friction, *e.g.*

$$\mathcal{T}_{advec} = \mathcal{T}_{fric}, \quad (13)$$

which occurs when L^* is

$$L_{fr} = \frac{h}{r} V^*. \quad (14)$$

L^* is thus the lesser of L_{Rh} and L_{fr} :

$$L^* = \begin{cases} L_{Rh} & \text{if } L_{Rh}/L_{fr} < 1 \\ L_{fr} & \text{if } L_{Rh}/L_{fr} > 1 \end{cases}. \quad (15)$$

4.2.4 Given V^* and L^* , what are F , $\overline{\rho}_y$ and L_{Rh}/L_{fr} ?

The scales for V^* and L^* can be substituted into (7) to obtain an estimate of F :

$$F = \begin{cases} r^{-1} \frac{\gamma g^2 h^4}{\rho_0^2 f^2} \overline{\rho}_y^{-3} & \text{if } L = L_{fr}, \text{ i.e. } L_{Rh}/L_{fr} \geq 1 \\ 2^{\frac{1}{2}} \frac{\partial h}{\partial y}^{-\frac{1}{2}} \frac{\gamma h^3 g^{\frac{3}{2}}}{\rho_0^{\frac{3}{2}} f^2} \overline{\rho}_y^{\frac{5}{2}} & \text{if } L = L_{Rh}, \text{ i.e. } L_{Rh}/L_{fr} \leq 1 \end{cases}. \quad (16)$$

F is already known from the *a priori* assumption that the cross-shelf density gradient is in steady-state (equation (5)), and so (16) can be solved for $\overline{\rho}_y$ (the third step of section 4):

$$\overline{\rho}_y = \begin{cases} r^{\frac{1}{3}} \frac{\rho_0^{\frac{2}{3}} f^{\frac{2}{3}}}{\gamma^{\frac{1}{3}} h^{\frac{4}{3}} g^{\frac{2}{3}}} F^{\frac{1}{3}} & \text{if } L_{Rh}/L_{fr} \geq 1 \\ \frac{\partial h}{\partial y}^{\frac{1}{5}} \frac{\rho_0^{\frac{3}{5}} f^{\frac{4}{5}}}{2^{\frac{1}{5}} \gamma^{\frac{2}{5}} h^{\frac{6}{5}} g^{\frac{3}{5}}} F^{\frac{2}{5}} & \text{if } L_{Rh}/L_{fr} \leq 1 \end{cases}, \quad (17)$$

which can be substituted into (9) and (14) to get L_{Rh}/L_{fr}

$$L_{Rh}/L_{fr} = \begin{cases} r^{\frac{5}{6}} \frac{\partial h}{\partial y}^{-\frac{1}{2}} \frac{2^{\frac{1}{2}} \gamma^{\frac{1}{6}} \rho_0^{\frac{1}{6}}}{g^{\frac{1}{6}} h^{\frac{1}{3}} f^{\frac{1}{3}}} F^{-\frac{1}{6}} & \text{if } L_{Rh}/L_{fr} \geq 1 \\ r \frac{\partial h}{\partial y}^{-\frac{3}{5}} \frac{2^{\frac{1}{2}} \gamma^{\frac{1}{5}} \rho_0^{\frac{1}{5}}}{g^{\frac{1}{5}} h^{\frac{2}{5}} f^{\frac{2}{5}}} F^{-\frac{1}{5}} & \text{if } L_{Rh}/L_{fr} \leq 1 \end{cases} \quad (18)$$

(Since both estimates of L_{Rh}/L_{fr} are equal to one at the same time, this is mathematically consistent.) These scales can be combined with (5) to find $\overline{\rho_y}$ and L_{Rh}/L_{fr} for a given bathymetry and cooling distribution.

Some implications of these scales are:

- Bottom friction does not affect the solution when $L_{Rh}/L_{fr} \leq 1$.
- Bottom slope does not affect the solution when $L_{Rh}/L_{fr} \geq 1$.
- The steady-state cross-shelf density gradient is only weakly dependent on the cross-shelf density flux F , and thus only weakly dependent on the surface buoyancy flux B .

These scales will be compared to numerical model runs, and the limits of their validity will be explored, in the next section.

5 Testing the scales in numerical models

The scale for the cross-shelf density gradient, (17), is tested by comparing (17) with the results of thirty-six model runs made with four different geometries and forcings. These model runs are also used to examine the parameter ranges over which the scalings are valid and to examine the transition from $L^* = L_{Rh}$ to $L^* = L_{fr}$.

Two of the geometries have the uniform bottom slopes and surface forcings illustrated in figure 1, one having a seaward boundary which transmits a buoyancy flux sufficient to balance the surface cooling, the “open wedge” geometry, and one having a seaward boundary through which no buoyancy is transmitted, the “closed wedge” geometry. The base cases of these model runs have a surface buoyancy flux of $7 \times 10^{-8} \text{ m}^2 \text{ s}^{-3}$, which is equivalent to a heat loss of 300 W m^{-2} from 3°C water or 170 W m^{-2} from 10°C water (the details of this conversion are given in the appendix). The base cases have a depth at the coastal wall of 10 meters and a bottom slope of 10^{-3} .

Two of the model geometries have the surface forcing limited to within 10 kilometers of the shore and an offshore wall through which there is no buoyancy flux. One geometry has a flat bottom, the “flat bottom” geometry, and the other a bottom of uniform slope, the “local cooling” geometry. The

bathymetry of the “local cooling” case is

$$h = \alpha(y - 23.3 \times 10^3 \text{ meters}) + 100 \text{ meters} \quad (19)$$

where α , the bottom slope, is 10^{-3} . The base case surface density forcing is $10^{-6} \text{ m}^2 \text{ s}^{-3}$ for both of these geometries. This would represent a tremendous heat flux if it only represented a heat flux; however, when brine rejection is included, it is a reasonable forcing for Arctic polyna events [*Cavaliere and Martin, 1994*]. All of the runs are summarized in table 1.

All of the model runs have a linear bottom drag law

$$\vec{\tau}_{\text{bottom}} = r\rho_0\vec{u} \quad (20)$$

and in the base cases $r = 4.5 \times 10^{-4} \text{ m s}^{-1}$. All of the models were run with a domain 160km wide in the cross shelf direction. The grid spacing was adjusted so that there were at least 5 eddies in the alongshelf direction and a typical eddy was resolved by at least 12 alongshelf gridpoints. The models were run until the cross-shelf density gradient, and the mean density of the domain in the “open wedge” runs, reached a steady-state. The models were then run for a further fifty to one hundred days while averages of the mean

density, density gradients, velocity variances, *etc.* were made. All averages were made at least one eddy length away from the coastal wall, and from the offshore wall if present. The parameters of each model run are given in table 1.

The first and most basic test of the model is to ask how the average cross-shelf density gradient in the model compares to the cross-shelf average of (17). To do so, a value of γ must be specified. γ , the correlation coefficient between the depth averaged density and the depth averaged cross-shelf velocity, is computed directly from time series of velocity and density taken from the numerical models, and an average value for each model run is presented in table 1. The value of γ differs systematically between the $L_{Rh}/L_{fr} > 1$ and $L_{Rh}/L_{fr} < 1$ runs. In comparing (17) to the model runs,

$$\gamma = \begin{cases} 0.45 & \text{if } L_{Rh}/L_{fr} \geq 1, \text{ i.e. } L^* = L_{fr} \\ 0.38 & \text{if } L_{Rh}/L_{fr} < 1, \text{ i.e. } L^* = L_{Rh} \end{cases} \quad (21)$$

is used. These γ 's were chosen by averaging the model run γ 's for all runs with $L_{Rh}/L_{fr} < 0.5$ (runs 1-6), and all runs with $L_{Rh}/L_{fr} > 3$ (runs 18-21 and f1-f15). Because the scales for V^* and L^* which make up (17) are only defined to within $O(1)$ constants, an $O(1)$ coefficient must be found to fit (17)

to the data (the scales V^* and L^* are examined in section 6). The best fit constant is found for each model run, and the best fit constants are averaged in the same manner as γ . When $L_{Rh}/L_{fr} > 3$, the average fitting constant is 0.98, and when $L_{Rh}/L_{fr} < 0.5$, the constant is 0.65, and so (17) becomes:

$$\overline{\rho_y} = \begin{cases} 0.98 r^{\frac{1}{3}} \frac{\rho_0^{\frac{2}{3}} f^{\frac{2}{3}}}{\gamma^{\frac{1}{3}} h^{\frac{4}{3}} g^{\frac{2}{3}}} F^{\frac{1}{3}} & \text{if } L_{Rh}/L_{fr} \geq 1 \\ 0.65 \frac{\partial h^{\frac{1}{5}}}{\partial y} \frac{\rho_0^{\frac{3}{5}} f^{\frac{4}{5}}}{2^{\frac{1}{5}} \gamma^{\frac{2}{5}} h^{\frac{6}{5}} g^{\frac{3}{5}}} F^{\frac{2}{5}} & \text{if } L_{Rh}/L_{fr} \leq 1 \end{cases}. \quad (22)$$

A comparison between cross-shelf average of (22) and the cross-shelf averaged density gradients in the numerical model runs is given in figure 7, and the demeaned depth averaged density anomaly for four of these model runs is also shown along with the cross-shelf integrals of (22) in figure 8. The choice of the constants in (22) does not make the comparison circular, for the scalings must still reproduce how $\overline{\rho_y}$ varies as the parameters are varied. Both figures indicate that, over a wide range of geometries, forcings, and bottom friction, (22) does well predicting how the cross-shelf density gradient changes in the numerical model as parameters are changed. (The derivation of the error bars in figure 7 and following is discussed in the appendix.)

Nonetheless, it is difficult to discern from figures 7 and 8 how well the

scalings predict the response of the model to changes in water depth, bottom friction, and cooling individually. It is also hard to explain from this plot the causes of the outliers in figure 7, the nature of the transition from $L_{Rh}/L_{fr} > 1$ to < 1 , and the limits of validity to (22). These will be addressed in turn below.

In figure 9, the changes in the cross-shelf averaged cross-shelf density gradient in the flat bottom cases are shown as the cooling, depth, bottom friction, and inertial frequency are varied- the expected percent changes from the base case cross-shelf density gradient are shown as a hollow outline, and the percent change in the numerical models are shown as the grey bars. The change in the density gradient is well predicted by the scalings, and these changes are resolved by the model, for all of the changes in the forcing and geometry except for halving of the water depth (runs f10-f12). Equation (22) systematically underestimates the change in the density gradient as the water depth is reduced from a hundred to fifty meters. This error may be due to the increased fraction of water column occupied by the bottom Ekman layer. The average Ekman depth in the model is about 10 meters (estimated as the height above the bottom where the RMS vertical stress falls below one tenth the RMS bottom stress). If, as an *ad hoc* correction, the water

depth in the scaling is reduced by this 10 meters, the comparisons in figure 9 improve significantly. Even without this *ad hoc* correction, the error in the scale for the cross-shelf density gradient is less than 40% when the depth is but 20 meters. In other runs, not shown here, it was found that the flow changes qualitatively and abruptly when $h/r \lesssim 4f^{-1}$ (about half a day at mid-latitude). The cold dense water is then transported by eddies trapped to the bottom boundary layer, and, over sloping bottoms, resembles the work of *Swaters* [1991]. In this limit, the scalings of the mean cross-shelf density gradient in (22) show no skill.

The transition from the $L^* = L_{fr}$ to the $L^* = L_{Rh}$ regimes leads to errors in the estimate of the cross-shelf density gradient, (22). This can be seen in figure 10, a plot of the percent error in the estimate as a function of the ratio of L_{Rh} to L_{fr} . The error in the $L^* = L_{fr}$ estimate approaches zero as the ratio becomes much less than one, and the error in the $L^* = L_{Rh}$ estimate approaches zero as the ratio becomes much greater than one. However, in the range $0.5 \leq L_{Rh}/L_{fr} \leq 3$, the scale for $L^* = L_{fr}$ overpredicts the cross-shelf density gradient by about 20 percent, and the scale for $L^* = L_{Rh}$ underpredicts the gradients by about 20 percent as the transition is made from one scale to the other and the physics is a mix of the two. It is for this

reason the $0.5 \leq L_{Rh}/L_{fr} \leq 3$ model runs are excluded from the averages used to compute γ in (21) and the constants in (22).

In this section, model runs have been presented in which L_{Rh}/L_{fr} varies from infinity down to 0.18, but no less. This is because there is another change in the dynamics at $L_{Rh}/L_{fr} \leq 0.15$. When L_{Rh}/L_{fr} is less than one, it can be interpreted as not only the ratio of the two length scales, but as the time scale of energy conversion from potential to the kinetic, \mathcal{T}_{advec} , to the time scale of kinetic energy dissipation, \mathcal{T}_{fric} . When this ratio falls below 0.15 and dissipation is relatively weak, the alongshelf (zonal) jets formed by the cascade to large scales [Rhines, 1977] acquire enough relative vorticity that they, not the topographical β , dominate the vorticity gradients that set L_{Rh} . To move the base “open wedge” case into the $L_{Rh}/L_{fr} < 0.15$ regime, one would have to increase the cooling by about 8000 times, decrease the friction by 6, increase the bottom slope by 20, or increase f by about 80, and so this regime is not addressed herein. This regime has been studied elsewhere because it is appropriate to the gas giants, Jupiter, Saturn, Neptune and Uranus. A review of the applicable literature can be found in Dowling [1995].

The estimate of $\overline{\rho_y}$ also breaks down when the cross-shelf buoyancy flux is carried by an overturning circulation, with dense water flowing offshore at

depth and less-dense water returning near the surface. This is similar to the Hadley cell circulation in the equatorial atmosphere, and has been studied in an oceanic context by *Condie and Rhines* [1994]. The size of the overturning cell is the radius of deformation [*Held and Hou*, 1980]. The vertical density difference is assumed to be the same as the horizontal density difference across the cell, the cross-shelf velocity to scale as $\sqrt{g'h}$ and the density of a water parcel crossing the shelf at the surface to increase in proportion with (1). The density difference then scales as $(\rho_0 B)(ghf)^{-1}$ and the width of the cell is proportional to $\sqrt{B/f^3}$, which is equal to or less than one kilometer for the base case runs presented here. Since the model domain is much larger than this, the overturning circulation hardly matters. (This derivation is similar to *James* [1994] and *Held and Hou* [1980]. An alternate derivation with the same result can be found in *Jones and Marshall* [1993].)

6 Testing the length and velocity scales

The scales for the cross-shelf density gradient contain scales for the depth averaged cross-shelf velocity anomaly and the length scales of the eddies. When these scales are compared with the numerical models they show systematic

errors which are functions of the Burger number, the square of the ratio of the internal radius of deformation in the numerical model to the eddy length scale observed in the model.

The ratio of the root mean square of the depth averaged cross-shelf velocity in the numerical model to the velocity scale V^* , V' , is shown as a function of the Burger number in figure 11. If the scaling for the cross-shelf velocity were completely successful, V' would be an $O(1)$ constant, but instead it increases nearly linearly with the Burger number.

The ratio of the cross-shelf eddy length in the model to the scale cross-shelf eddy length, L' , shows a complementary relation when plotted against the Burger number— it scales as approximately one over the Burger number less six, forming a rough hyperbola. (The same result is found for the sloping bottom cases, though the analysis is complicated by the change in Burger number across the shelf.)

These results agree with some quasigeostrophic energetic arguments of *Pedlosky* [1987] and *Visbeck et al.* [1996], and with the work of *Held and Larichev* [1995] and *Shepherd* [1988]. Unfortunately this cannot be used to improve the scalings for V^* and L^* , for I have been unable to find a satisfactory *a priori* scaling for the vertical stratification and thus the radius

of deformation.

Fortunately for the success of the estimate of the cross-shelf density gradient, the errors in the scales for the cross-shelf velocity and the eddy length scale are such that their product is nearly constant, and thus the scale for VL is much better than the scale for either alone. It is this product which enters into the scale for the cross-shelf buoyancy flux, (16), and hence into the estimate of the cross-shelf density gradient.

The deficiencies in the scales for V^* and L^* clearly point out their *ad hoc* nature, and indicate a direction that future work must take.

7 Conclusion

The cross-shelf buoyancy flux driven by a given cross-shelf density gradient is found for a coastal ocean with no mean alongshore variation in forcing or geometry (16). It is found under the assumption that the baroclinic instabilities in the flow field have grown to form eddies, and that the cascade of these eddies to larger length scales has reached equilibrium. The resulting length scale of the eddies is estimated to be the lesser of the Rhines arrest scale (9) or a friction arrest scale (14). The strength of the cross-shelf buoyancy flux

is found to depend on bottom friction and slope, modifying the results of CG, at least in the limit of polynas with a large alongshore extent.

This relation between the cross-shelf density gradient and the cross-shelf heat flux is then used to estimate the steady-state cross-shelf density gradient of a continental shelf exposed to steady winter-time cooling (17). The steady-state is attained when the sum of the divergence of the cross-shelf heat flux and the surface cooling divided by water depth is everywhere the same, so that the density of the water increases everywhere at the same rate, leaving the cross-shelf density gradient unchanged (5). The steady-state cross-shelf density gradient exists even when the offshore boundary condition precludes the existence of a steady-state density.

The steady-state cross-shelf density gradient scaling is tested in numerical models of the continental shelf run over a broad range of parameters (table 1), and it is found that the scaling predicts the cross-shelf density gradient well (figure 7). In model runs whose parameters are similar to those of the Mid-Atlantic Bight, the steady-state cross-shelf density gradient is achieved in less than a winter (figure 3).

Because the scalings for the cross-shelf heat flux and the cross-shelf density gradients are only valid when there is at least weak bottom friction, they

will not be directly relevant to the deep ocean and thus the work of VMJ. However, the result that the interaction of eddies is important to the evolution of broad regions of instability is likely to hold even in the absence of bottom friction and suggests further extensions to VMJ and *Visbeck et al.* [1997].

The effect of wind-driven boundary-layer currents forced by the wind on the eddies has not been considered. Since these currents can be considerable, their effect on the eddies must be considered in any more complete theory.

Acknowledgments

This paper would have been impossible without Ken Brink's many readings and numerous pieces of scientific advice, and the many pieces of good advice given to me by my committee- Paola Rizzoli, Steve Lentz, John Trowbridge, and Glen Gawarkiewicz. Peter Franks was kind enough to let me work on this while doing my postdoctoral work. Many talks with Mike Spall helped to clarify my thinking, and Dave Chapman was kind enough to carefully read and comment on the manuscript. Melissa Bowen bravely suffered through an early draft. Two anonymous reviewers significantly improved this work

with their comments. The work was funded by an Office of Naval Research fellowship and and Office of Naval Research AASERT fellowship, N00014-95-1-0746.

8 Appendix

The numerical model is SPEM 5.1, an enhanced version of the primitive equation model described in *Hedstrom* [1994]. This version of SPEM uses finite differences in the vertical and an implicit mixing scheme. The model is now built on a full 3D Arakawa C grid and has a rigid lid.

The model uses a modified sigma coordinate system in the vertical, in which the vertical resolution near the top and bottom is kept constant while the interior vertical resolution scales with the water depth [*Song and Haidvogel*, 1994]. The model was run with thirty levels in the vertical, concentrating eight levels in both the top and bottom ten meters in order to resolve the boundary layers. The cross-shelf resolution was 2 km, and the alongshelf resolution was between 2 and 4 km, as required to resolve eddies with at least 12 grid-points.

The numerics of the model were changed in order to improve the com-

putational speed by a factor of three by running the implicit vertical mixing scheme at a shorter timestep than the rest of the model. This is necessary because of the extremely high diffusivities needed to model convection. See *Pringle* [1998] for details of the changes to the code.

The seaward boundary is a free slip vertical wall in the $F_0 = 0$ cases. When the seaward boundary is required to supply an F_0 capable of balancing the surface cooling, the boundary is modeled with a 15 km seaward extension to the model domain in which the density is relaxed back to ρ_0 with a time scale of 3 days. The bottom is flat in this region. The horizontal eddy viscosity in that region is raised to 20 m s^{-2} in the boundary region to dissipate eddy momentum.

The model was run with the Pacanowski and Philander (1981) Richardson number dependent mixing scheme. This mixing scheme has given good results in previous studies [*Allen and Newberger*, 1996; *Nunes Vas and Simpson*, 1994] and is described in *Pringle* [1998]. Convective adjustment is handled by an enhanced eddy diffusivity:

$$A_{convection} = \nu_{convection} = \frac{1}{4}w^*h = \frac{1}{4}h^{\frac{4}{3}}B^{\frac{1}{3}}. \quad (23)$$

This convection parameterization is related to data and more sophisticated mixing schemes in *Pringle* [1998].

The heat flux at the surface has been converted to a buoyancy flux for the model runs described here. If one assumes a linear equation of state, this is straightforward. Multiplying the boundary condition on temperature

$$\nu T_z = \frac{F}{C_p \rho_0} \quad @z = 0, \quad (24)$$

by the thermal expansion coefficient, $\alpha = \frac{\partial \rho}{\partial T}$, gives a boundary condition on density of

$$\nu \rho_z = \rho_0 B/g \quad @z = 0, \quad (25)$$

where F is the heat flux in watts per meter squared and B the equivalent surface buoyancy flux. α is a strong function of temperature, unlike C_p . For a given heat flux, the equivalent buoyancy flux is 2.2 times greater at 5°C than at 0 °C. Figure 12 is a plot of the equivalent buoyancy flux for a heat loss of 300 W m⁻² as a function of water temperature. A buoyancy flux of 7×10^{-8} m²s⁻³ is used for the base sloping bottom cases, which is equivalent to a heat loss of 300 W m⁻² from 3 °C water or 170 W m⁻² from 10 °C water.

The surface buoyancy flux is fourteen times greater in the base flat bottom cases to account for increased buoyancy fluxes driven by brine rejection.

Error bars on the mean cross-shelf density gradient in the numerical models are computed from the standard deviation and degrees of freedom of a time series of the cross-shelf average cross-shelf density gradient computed every model day once the model had reached steady state. There is also a systematic error in cross-shelf density gradient because the domain is periodic in the alongshelf direction, and thus there must be an integer number of eddies in the alongshelf direction. This error is estimated and included in the error bars by calculating what effect a $\pm 0.5 L_{model}^2 L_{domain}^{-1}$ change in the lengthscale L^* would have on the cross-shelf density gradient scale, where L_{model} is the eddy length observed in the model, and L_{domain} is the alongshelf size of the domain. No estimate of the error induced by cross-shelf quantization was made, since that would be an error in the estimate of the cross-shelf density gradient, not the numerical model.

9 Bibliography

- Allen, J. S., and P. A. Newberger, Downwelling Circulation on the Oregon Continental Shelf. Part I: Response to Idealized Forcing, *J. Phys. Oceanogr.*, *26*, 2011–2035, 1996.
- Blumsack, S. L., and P. J. Gierasch, Mars: The Effects of Topography on Baroclinic Instability, *J. Atmos. Sci.*, *29*, 1081–1089, 1972.
- Brown, W. S., and R. C. Beardsley, Winter Circulation in the Western Gulf of Maine: Part I cooling and Water Mass Formation, *J. Phys. Oceanogr.*, *8*(2), 265–277, 1978.
- Cavalieri, D. J., and S. Martin, The Contribution Of Alaskan, Siberian, And Canadian Coastal Polynyas To The Cold Halocline Layer Of The Arctic Ocean., *J. Geophys. Res.*, *15*, 18343–18362, 1994.
- Chapman, D. C., Setting the Scales of the Ocean Response to Isolated Convection, *J. Phys. Oceanogr.*, *28*, 606–620, 1998.
- Chapman, D. C., and G. Gawarkiewicz, Shallow Convection and Buoyancy Equilibration in an Idealized Coastal Polynya , *J. Phys. Oceanogr.*, *27*(4), 555–566, 1997.

- Condie, S. A., and P. B. Rhines, Topographic Hadley Cells, *J. Fluid Mech.*, 280, 349–368, 1994.
- Davis, R. E., Modeling Eddy Transport of Passive Tracers, *J. Marine Res.*, 45, 635–666, 1987.
- Dowling, T. E., Dynamics of Jovian Atmospheres, *Ann. Rev. Fluid Mech.*, 27, 293–334, 1995.
- Hedstrom, K., SPEM 3.0 User’s Guide, Inst. for Naval Oceanography, Technical Report SR-1, 1994.
- Held, I., and A. Y. Hou, Nonlinear Axially Symetric Circulation in a Nearly Inviscid Atmosphere, *J. Atmos. Sci.*, 37, 515–533, 1980.
- Held, I. M., and V. D. Larichev, A Scaling Theory for Horizontally Homogeneous, Baroclinically Unstable Flow on a Beta Plane, *J. Atmos. Sci.*, 53(7), 946–952, 1995.
- Hogg, N. G., and H. M. Stommel, The Heton, an Elementary Interaction Between Discrete Baroclinic Geostrophic Vortices and its Implications Concerning Eddy Heat Flow, *Proc. Roy. Soc. Lond.*, 397, 1–20, 1985.
- James, I. N., *Introduction to Circulating Atmospheres*, Cambridge University Press, New York, 1994.

- Jones, H., and J. Marshall, Convection with rotation in a neutral ocean: a study of open-ocean deep convection, *J. Phys. Oceanogr.*, *23*, 1009–1039, 1993.
- Kevorkian, J., *Partial Differential Equations – Analytical solution techniques*, Wadsworth & Brooks/Cole, Pacific Grove, 1990.
- Killworth, P. D., On the parameterisation of eddy transfer. Part II: Tests with a channel model, *J. Marine Res.*, *In Press*, 1998.
- LaCasce, J. H., Baroclinic Vortices Over a Sloping Bottom, MIT/WHOI Joint Program, PhD Thesis, 1996.
- Legg, S., H. Jones, and M. Visbeck, A heton perspective of baroclinic eddy transfer in localized open ocean convection, *J. Phys. Oceanogr.*, *26*, 2251–2266, 1996.
- Legg, S., J. McWilliams, and J. Gao, Localization of Deep Ocean Convection by a Mesoscale Eddy, *J. Phys. Oceanogr.*, *28*, 944–970, 1998.
- Mountain, D. G., G. A. Stout, and R. C. Beardsley, Surface Heat Flux in the Gulf of Maine, *Deep Sea Res.*, *43(II)*, 1533–1546, 1996.
- Nunes Vas, R. A., and J. H. Simpson, Turbulence Closure Modeling of Estuarine Stratification, *J. Geophys. Res.*, *99(C8)*, 16143–16160, 1994.

- Pedlosky, J., *Geophysical Fluid Dynamics* (second edition), Springer-Verlag, New York, 1987.
- Pringle, J. M., Cooling and internal waves over the continental shelf, MIT/WHOI Joint Program, PhD Thesis, 1998.
- Rhines, P. B., The Dynamics of Unsteady Currents, in *The Sea*, edited by E. A. Goldberg, I. N. McCave, J. J. O'Brien and J. H. Steele, 6, pp. 189–318, Wiley, 1977.
- Shepherd, T. G., Nonlinear Saturation of Baroclinic Instability. Part I: The Two-Layer Model, *J. Atmos. Sci.*, 45(14), 2014–2025, 1988.
- Song, Y., and D. Haidvogel, A Semi-Implicit Ocean Circulation Model Using a Generalized Topography-Following Coordinate System, *J. Comp. Phys.*, 115, 228–244, 1994.
- Spall, M. A., and D. C. Chapman, On the Efficiency of Baroclinic Eddy Heat Transport Across Narrow Fronts, *J. Phys. Oceanogr.*, 28(11), 2275–2287, 1998.
- St-Maurice, J-P., and G. Veronis, A Multi-Scaling Analysis of the Spin-up Problem, *J. Fluid Mech.*, 68, 417–445, 1975.

- Stone, P. H., A Simplified Radiative-Dynamical Model for the Static Stability of Rotating Atmospheres, *J. Atmos. Sci.*, 29(3), 405–418, 1972.
- Swaters, G. E., On the Baroclinic Instability of Cold-Core Coupled Density Fronts on a Sloping Continental Shelf, *J. Fluid Mech.*, 224, 361–382, 1991.
- Visbeck, M., J. Marshall, T. Haine, and M. Spall, Specification of Eddy Transfer Coefficients in Coarse Resolution Ocean Circulation Models, *J. Phys. Oceanogr.*, 27, 381–402, 1997.
- Visbeck, M., J. Marshall, and H. Jones, Dynamics of Isolated convective Regions in the Ocean, *J. Phys. Oceanogr.*, 26, 1721–1734, 1996.

| run number | geometry | γ | L_{Rh}/L_{fr} | Δx | change from base case |
|------------|---------------|----------|-----------------|------------|--------------------------------|
| f1 | flat bottom | 0.45 | ∞ | 2 | base case |
| f2 | flat bottom | 0.47 | ∞ | 2 | $h/2$ |
| f3 | flat bottom | 0.43 | ∞ | 2 | $2h$ |
| f4 | flat bottom | 0.43 | ∞ | 4 | $3h$ |
| f5 | flat bottom | 0.47 | ∞ | 4 | $4h$ |
| f6 | flat bottom | 0.48 | ∞ | 2 | $r/4$ |
| f7 | flat bottom | 0.44 | ∞ | 2 | $r/2$ |
| f8 | flat bottom | 0.39 | ∞ | 2 | $2r$ |
| f9 | flat bottom | 0.40 | ∞ | 2 | $Q/4$ |
| f10 | flat bottom | 0.44 | ∞ | 2 | $Q/2$ |
| f11 | flat bottom | 0.47 | ∞ | 2 | $2Q$ |
| f12 | flat bottom | 0.50 | ∞ | 2 | $h/2, r/2$ |
| f13 | flat bottom | 0.51 | ∞ | 2 | $h/2, r/4$ |
| f14 | flat bottom | 0.52 | ∞ | 2 | $h/2, r/10$ |
| f15 | flat bottom | 0.45 | ∞ | 2 | $3h/4, 2f$ |
| 1 | local cooling | 0.31 | 0.18 | 2 | $2Q, 2f, 1/2r$ |
| 2 | local cooling | 0.38 | 0.22 | 4 | slope $\times 5$, depth+26.5m |
| 3 | local cooling | 0.38 | 0.29 | 4 | $r/4$ |
| 4 | open wedge | 0.40 | 0.31 | 2 | $r/2$ |
| 5 | closed wedge | 0.43 | 0.37 | 2 | $r/2$ |
| 6 | local cooling | 0.38 | 0.43 | 4 | $r/2$ |
| 7 | open wedge | 0.45 | 0.47 | 2 | $2f$ |
| 8 | local cooling | 0.34 | 0.52 | 4 | double slope |
| 9 | open wedge | 0.40 | 0.62 | 2 | base case |
| 10 | closed wedge | 0.45 | 0.63 | 2 | $2Q$ |
| 11 | closed wedge | 0.47 | 0.73 | 2 | base case |
| 12 | local cooling | 0.38 | 0.87 | 4 | base case |
| 13 | local cooling | 0.39 | 1.30 | 2 | slope/1.6 |
| 14 | local cooling | 0.42 | 1.39 | 2 | slope/2 |
| 15 | closed wedge | 0.47 | 1.40 | 2 | slope/2 |
| 16 | local cooling | 0.37 | 1.70 | 4 | $2r$ |
| 17 | local cooling | 0.42 | 2.30 | 2 | slope/5 |
| 18 | local cooling | 0.42 | 3.20 | 2 | slope/10 |
| 19 | local cooling | 0.45 | 5.05 | 2 | slope/24 |
| 20 | local cooling | 0.44 | 8.00 | 2 | slope/60 |
| 21 | local cooling | 0.45 | 13.1 | 2 | slope/160 |

Table 1: A table of the geometry and changes from the base case for the model runs enumerated in figures 10 and 9. γ is the correlation between the depth averaged v and ρ fields observed in the model. L_{Rh}/L_{fr} is an average of (18) over the model domain, and is calculated from the forcing and geometry. Δx is the grid spacing in kilometers. $2Q$ means double the cooling of the base case, $2f$ means double the rotation rate, *etc.* r is bottom friction, ‘‘Slope’’ is the bottom slope, h is the water depth.

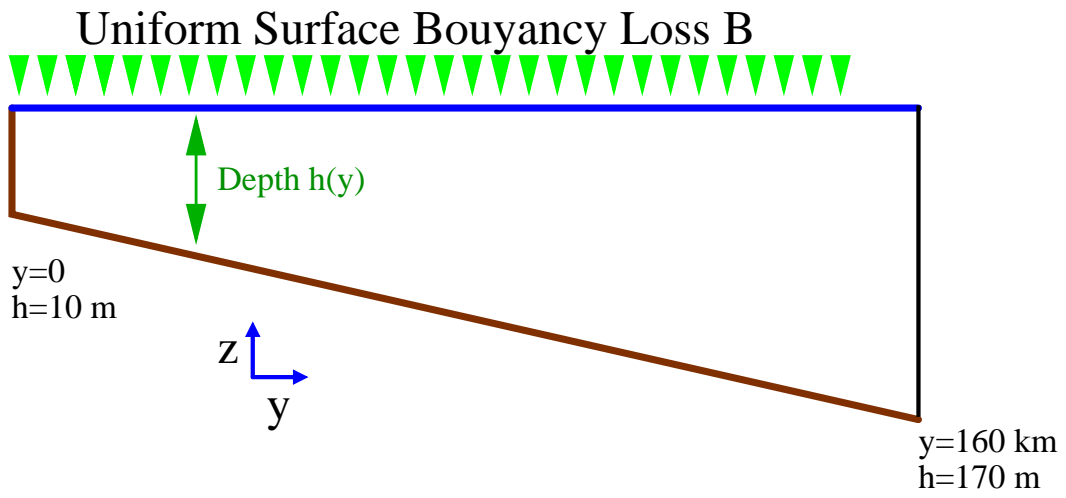


Figure 1: The geometry and forcing of the model described in section 2.

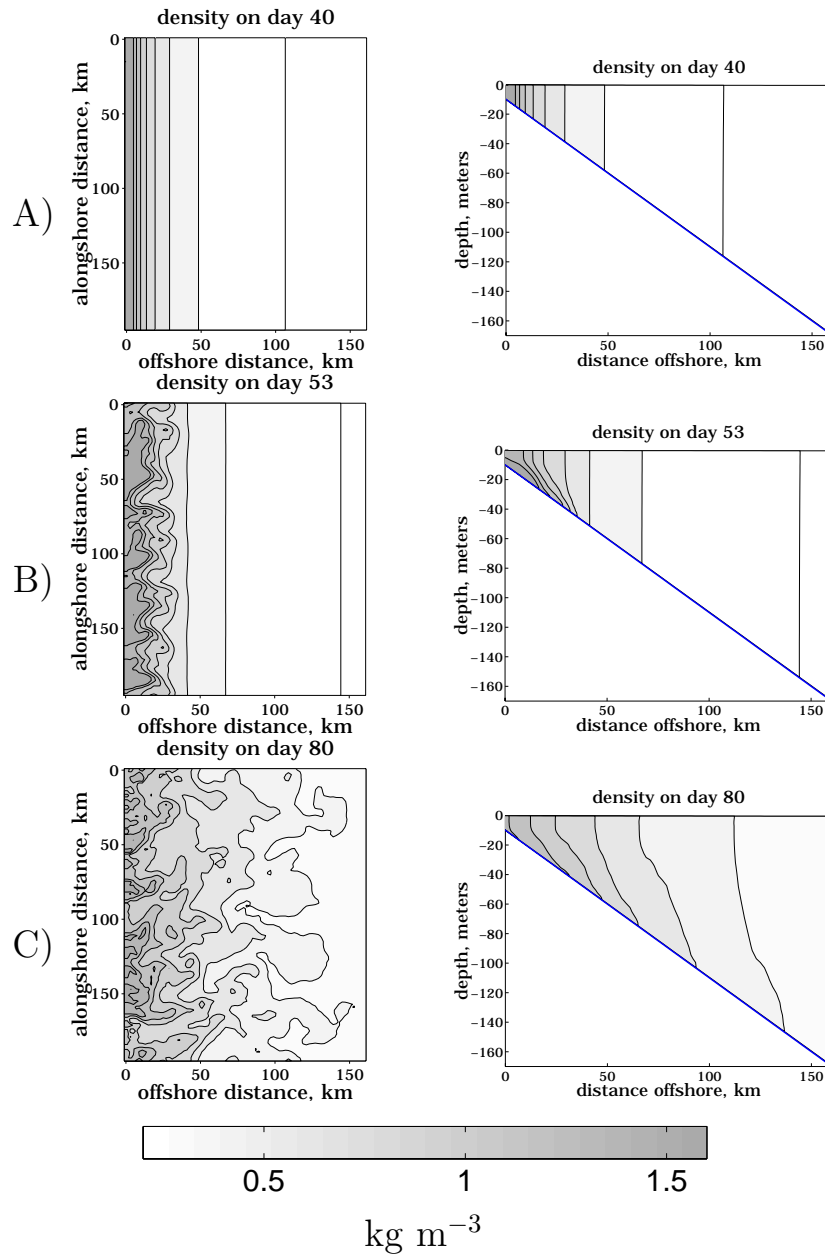


Figure 2: The lefthand plots are of the depth averaged density, the righthand of the alongshelf averaged density. Panel A is from 40 days after the start of cooling, panel B after 53 days, and panel C after 80 days.

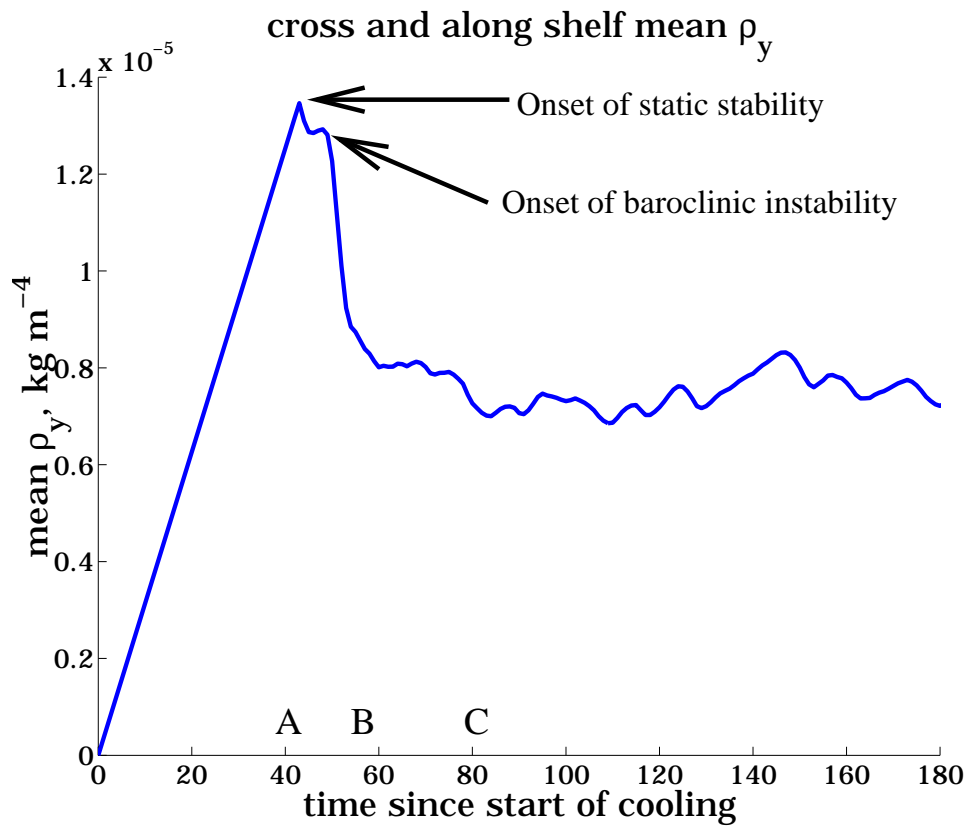


Figure 3: The cross-shelf averaged cross-shelf gradient in the depth and alongshelf averaged density. The average is computed across the entire model domain. The letters on the abscissa refer to the panels of figure 2.

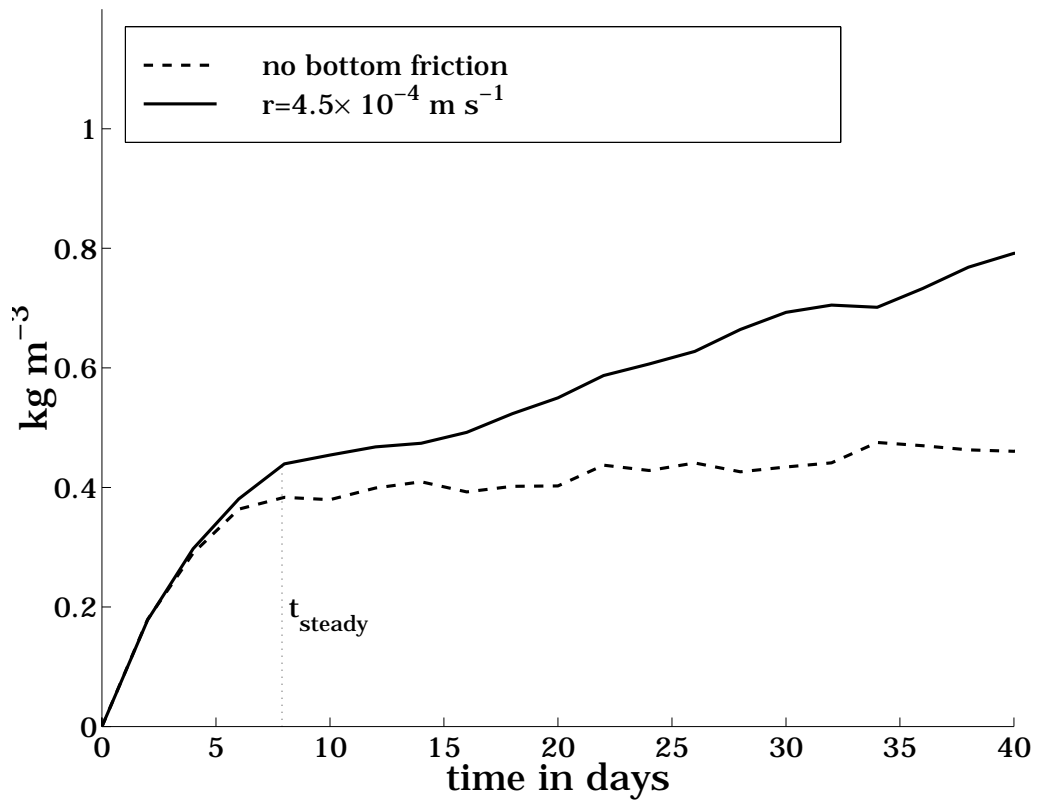


Figure 4: The average density of the cooling region for two numerical models with cooling limited to within 10km of the coast, one with bottom friction, one without. Each curve is the result of the average of four model runs, each initialized with an RMS noise in the density field of $10^{-3} \text{ kg m}^{-3}$.

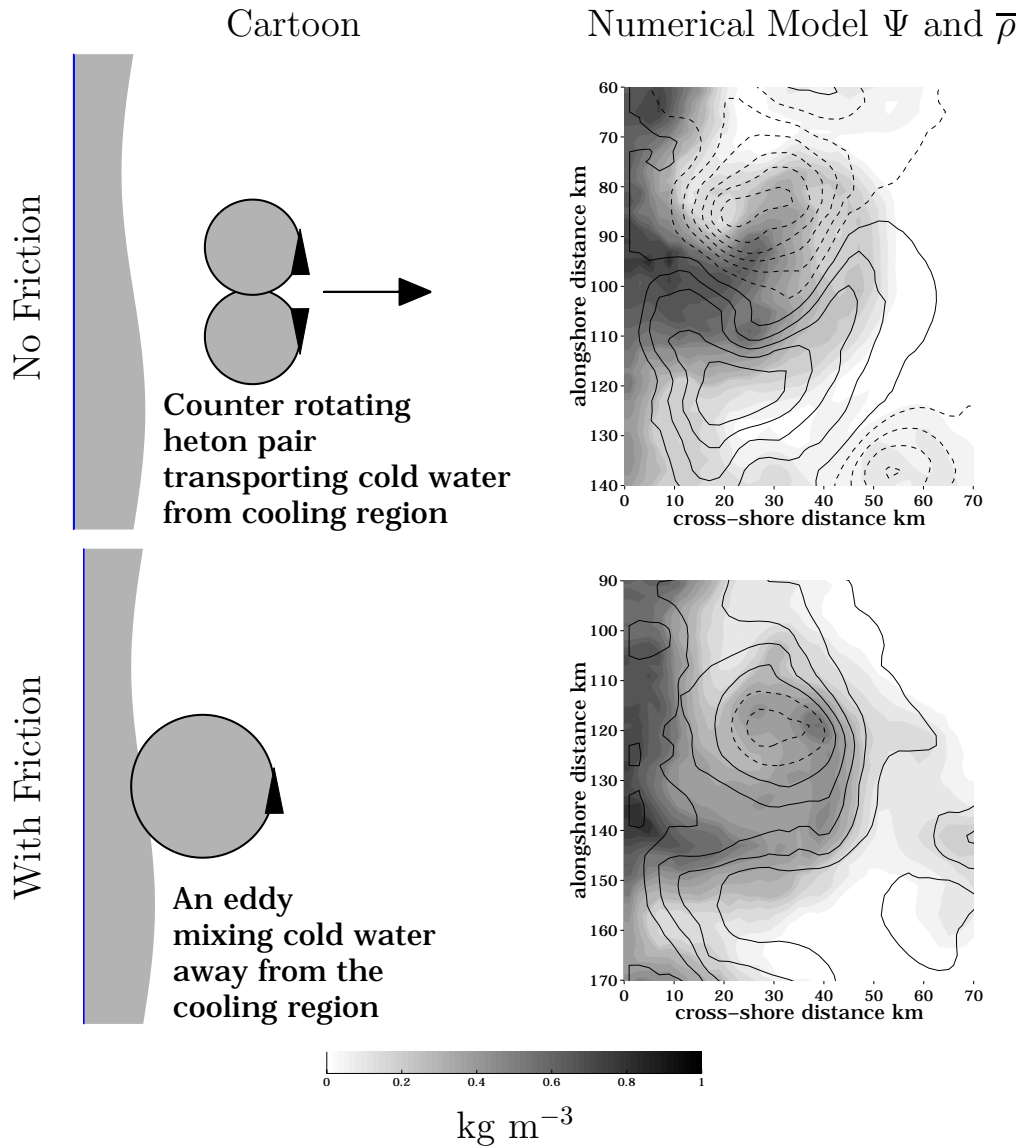


Figure 5: Two cartoons illustrating eddy transport of heat offshore in a model with and without bottom friction, and plots of the barotropic streamfunction overlaying the depth averaged density from day 20 of two corresponding model runs. Negative streamlines are dashed, and the contour interval is $5 \times 10^4 \text{ m}^3 \text{ s}^{-1}$.

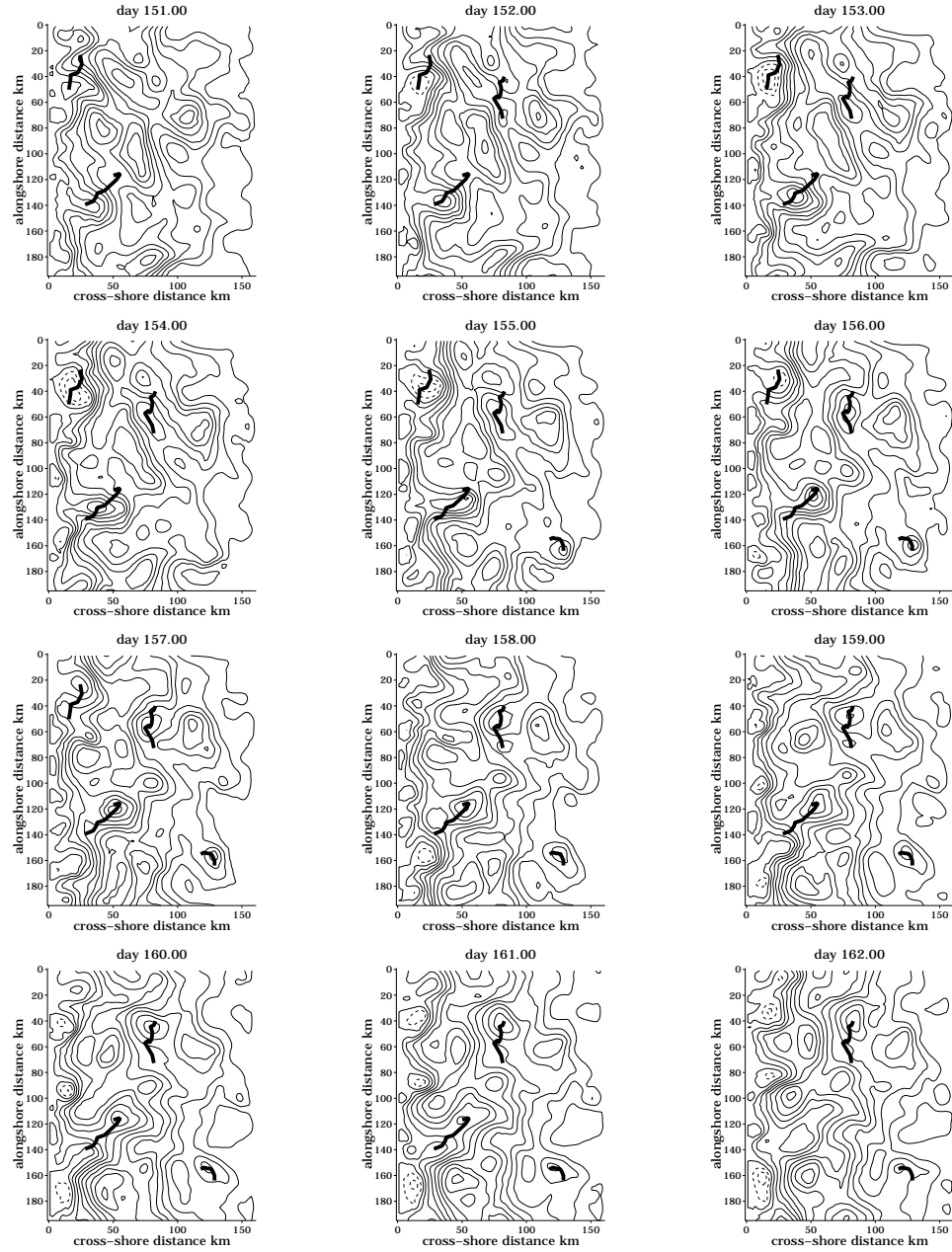


Figure 6: The paths of four eddies tracked for 12 days (heavy line) overlaying the transport streamfunction from the steady-state of the case with bottom friction. The eddy locations are defined by the local maximum or minimum in streamfunction. The paths are only plotted while the eddies exist. The contour interval for the streamfunction is $5 \times 10^4 \text{ m}^3 \text{ s}^{-1}$.

Mean Cross-Shelf density gradient, $\times 10^{-5} \text{ kg m}^{-4}$

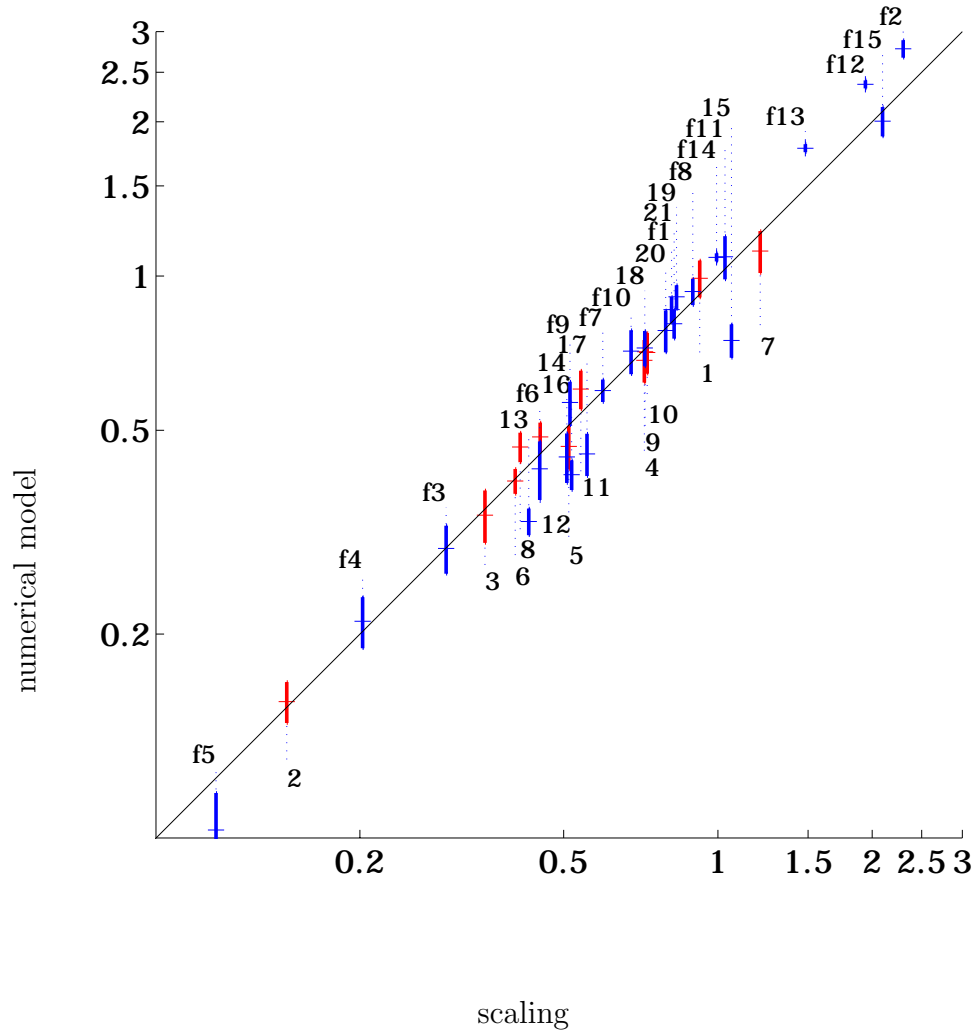


Figure 7: A comparison of the cross-shelf averaged cross-shelf density gradient predicted by (22) and those in the numerical models. Each point is labeled by the model number from table 1. The labels are above the diagonal when $L_{Rh}/L_{fr} > 1$ and below when $L_{Rh}/L_{fr} < 1$. The error bars are ± 1 standard deviation, and their calculation is described in the appendix.

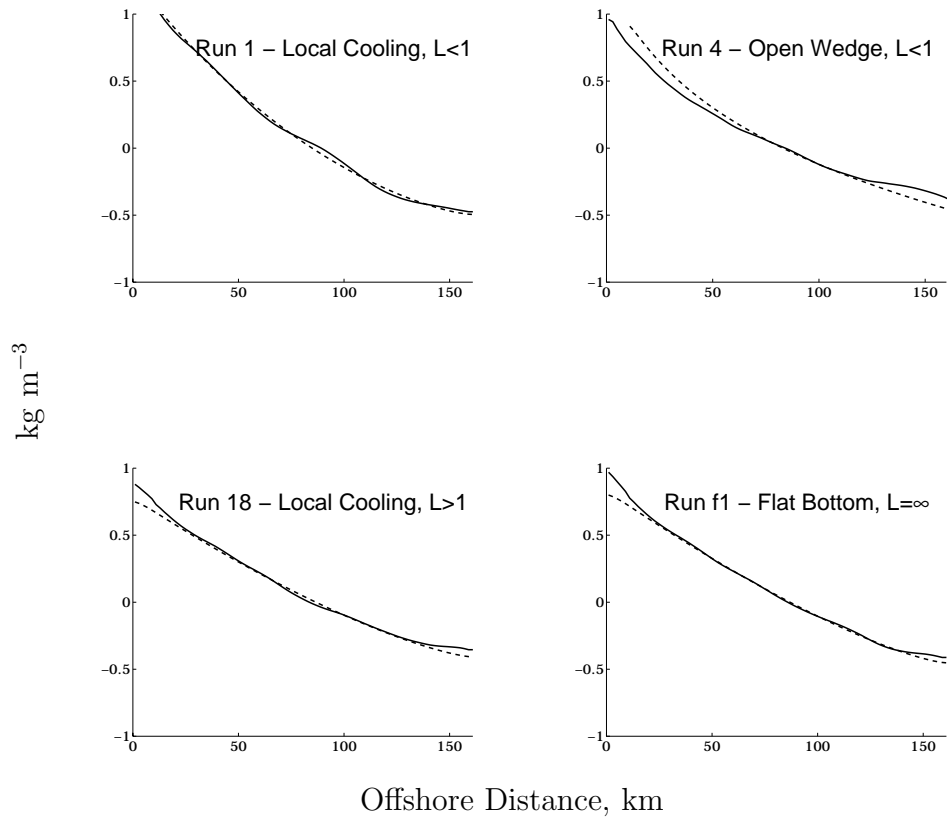


Figure 8: The alongshore and depth averaged steady-state density anomaly from the numerical model runs (solid line) and the cross-shelf integral of (22) (dashed line). The run number is on each panel.

The Boxes are the Predictions of the Scaling of the Percent Change of $\partial\bar{p}/\partial y$ From the Base Case, and the Gray Bars are the Numerical Model Results

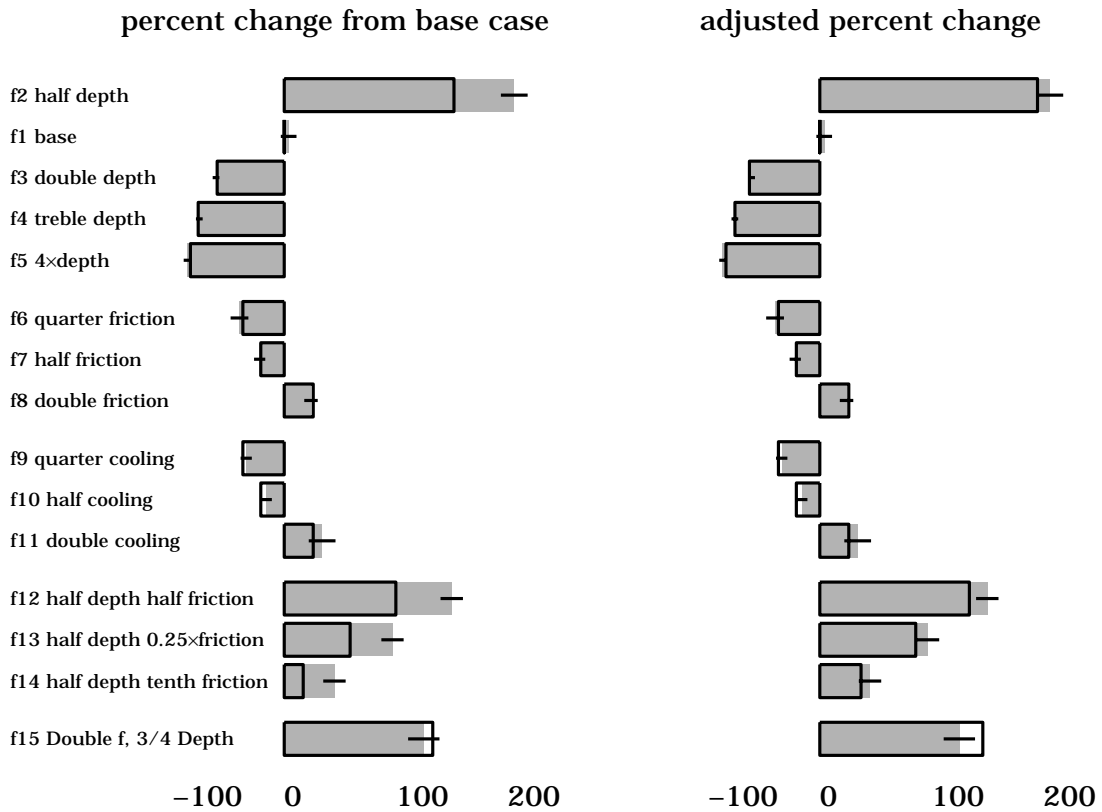


Figure 9: The percent change of the cross-shelf averaged cross-shelf density gradient from the base case. The hollow boxes are the predictions from the scaling, the gray filling the results from the numerical model. The horizontal lines are one standard deviation error bars. The righthand side has been adjusted for a finite Ekman depth, the lefthand side has not.

Percent Error in Estimate of Steady-State Cross-Shelf Density Gradient in Equation (22)

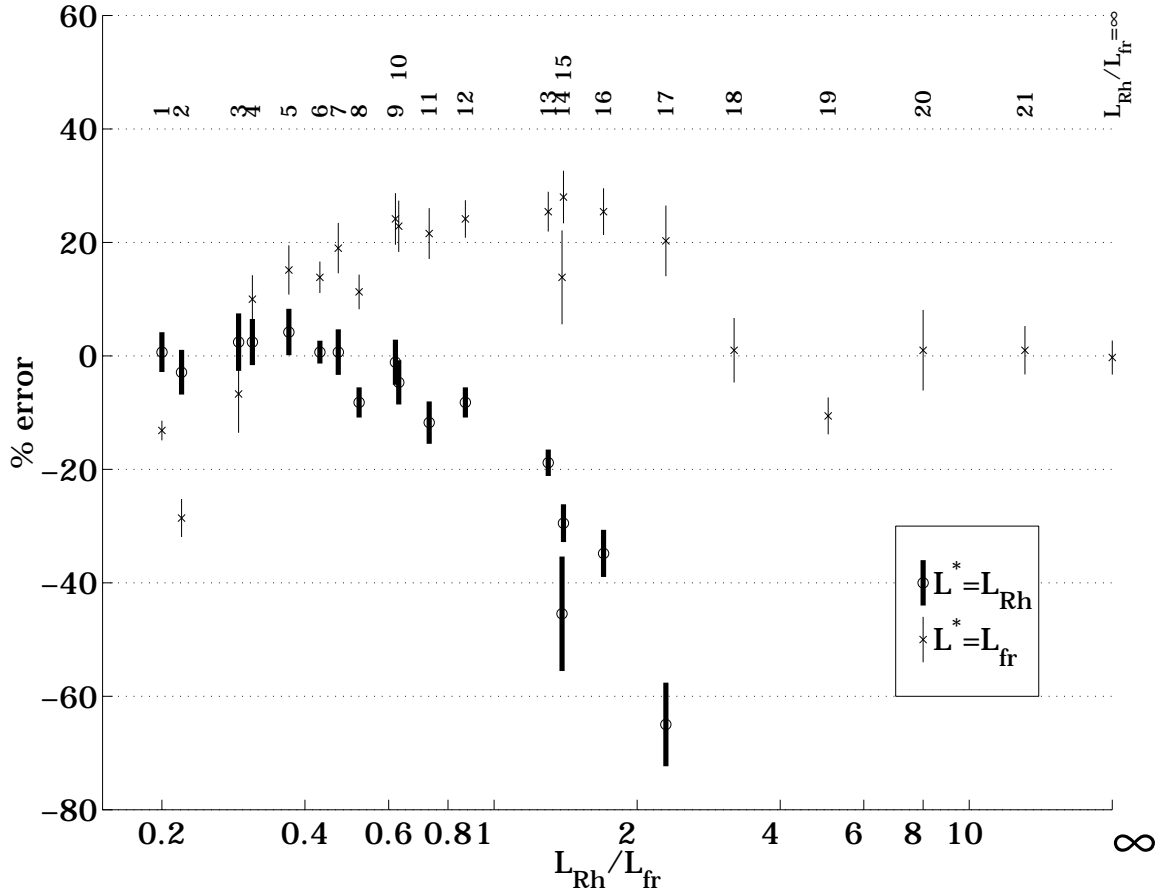


Figure 10: The error in the prediction of (22) when compared to the results of the numerical model. γ is computed from the model. The fit for $L_{Rh}/L_{fr} = \infty$ is the average error of the flat bottom runs, except for the $h = 50\text{m}$ runs. The error bars are ± 1 standard error as described in the appendix, and the model runs are keyed above the data points.

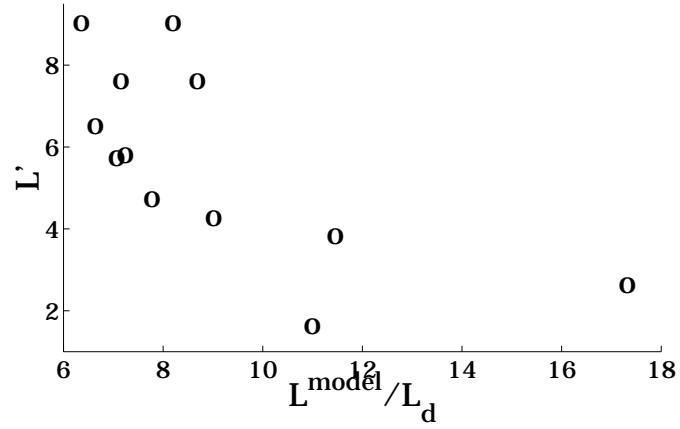
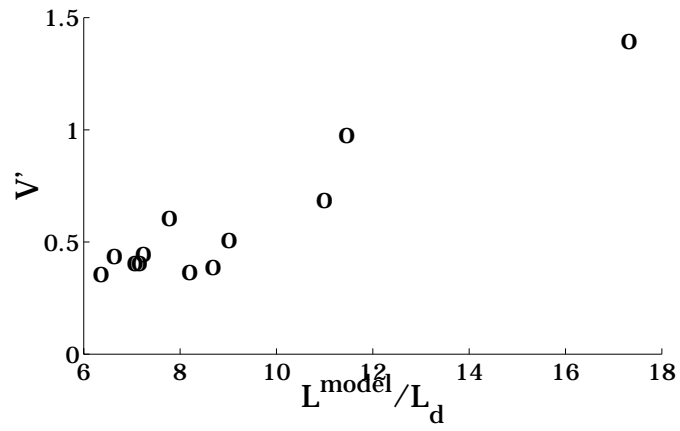


Figure 11: V' and L' against the square root of the inverse Burger number, L^{model}/L_d , as computed from the flat bottom model runs.

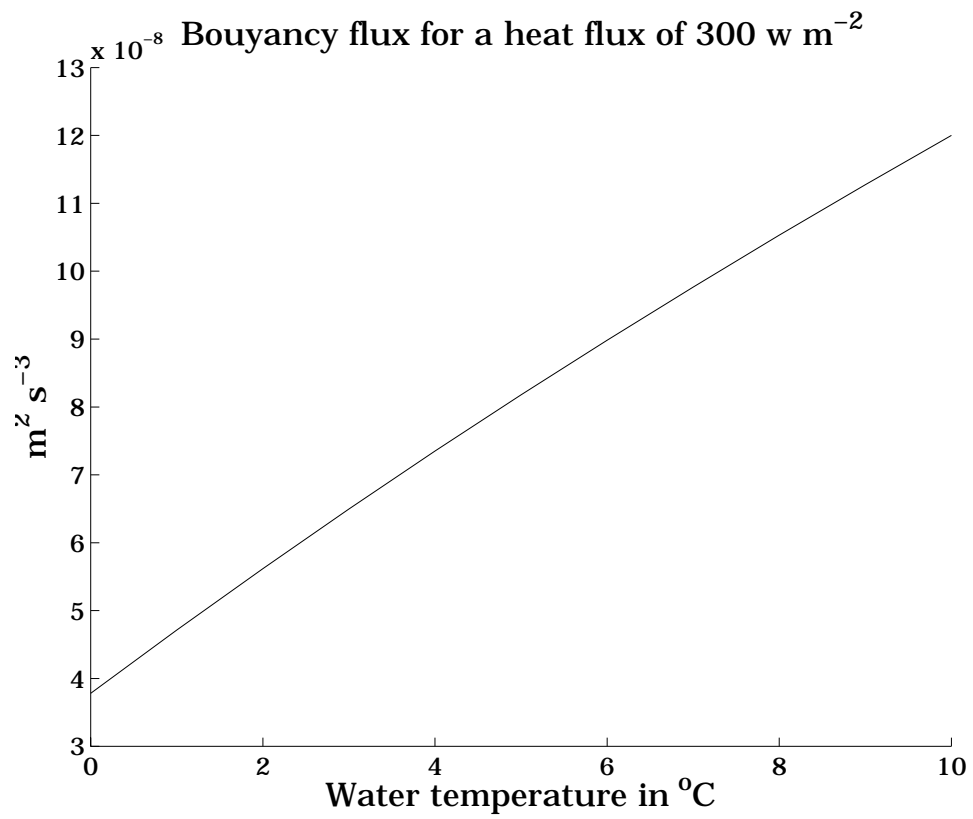


Figure 12: The equivalent buoyancy flux for a heat flux of 300 Watts per meter squared as a function of water temperature.